A quintuple star system containing two eclipsing binaries.

Rappaport, S.; Lehmann, H.; Kalomeni, B.; Borkovits, T.; Latham, D.; Bieryla, A.; Ngo, H.; Mawet, D.; Howell, S.; Horch, E.; ...

Permanent link / Trajna poveznica: https://urn.nsk.hr/urn:nbn:hr:217:606304

Download date / Datum preuzimanja: **2024-07-16**

A quintuple star system containing two eclipsing binaries

S. Rappaport,[1]* H. Lehmann,[2] B. Kalomeni,[1,3] T. Borkovits,[4] D. Latham,[5]
A. Bieryla,[5] H. Ngo,[6] D. Mawet,[7,8] S. Howell,[9] E. Horch,[10] T. L. Jacobs,[11]
D. LaCourse,[12] Á. Sódor,[13] A. Vanderburg[5] and K. Pavlovski[14]

[1]*Department of Physics, and Kavli Institute for Astrophysics and Space Research, Massachusetts Institute of Technology, Cambridge, MA 02139, USA*
[2]*Thüringer Landessternwarte Tautenburg, Sternwarte 5, D-07778 Tautenburg, Germany*
[3]*Department of Astronomy and Space Sciences, Ege University, 35100 İzmir, Turkey*
[4]*Baja Astronomical Observatory of Szeged University, Szegedi út, Kt. 766, H-6500 Baja, Hungary*
[5]*Harvard–Smithsonian Center for Astrophysics, 60 Garden Street, Cambridge, MA 02138, USA*
[6]*California Institute of Technology, Division of Geological and Planetary Sciences, 1200 E California Blvd MC 150-21, Pasadena, CA 91125, USA*
[7]*California Institute of Technology, Astronomy Department MC 249-17, 1200 E. California Blvd, Pasadena, CA 91125, USA*
[8]*Jet Propulsion Laboratory, California Institute of Technology, 4800 Oak Grove Drive, Pasadena, CA 91109, USA*
[9]*Kepler and K2 Missions, NASA Ames Research Center, PO Box 1, M/S 244-30, Moffett Field, CA 94035, USA*
[10]*Department of Physics, Southern Connecticut State University, New Haven, CT 06515, USA*
[11]*12812 SE 69th Place, Bellevue, WA 98006, USA*
[12]*7507 52nd Place NE Marysville, WA 98270, USA*
[13]*Konkoly Observatory, MTA CSFK, Konkoly Thege M. út 15–17, H-1121 Budapest, Hungary*
[14]*Department of Physics, University of Zagreb, Bijenicka cesta 32, 10000 Zagreb, Croatia*

ABSTRACT

We present a quintuple star system that contains two eclipsing binaries. The unusual architecture includes two stellar images separated by 11 arcsec on the sky: EPIC 212651213 and EPIC 212651234. The more easterly image (212651213) actually hosts both eclipsing binaries which are resolved within that image at 0.09 arcsec, while the westerly image (212651234) appears to be single in adaptive optics (AO), speckle imaging, and radial velocity (RV) studies. The 'A' binary is circular with a 5.1-d period, while the 'B' binary is eccentric with a 13.1-d period. The γ velocities of the A and B binaries are different by $\sim$10 km s^{-1}. That, coupled with their resolved projected separation of 0.09 arcsec, indicates that the orbital period and separation of the 'C' binary (consisting of A orbiting B) are $\simeq$65 yr and $\simeq$25 au, respectively, under the simplifying assumption of a circular orbit. Motion within the C orbit should be discernible via future RV, AO, and speckle imaging studies within a couple of years. The C system (i.e. 212651213) has an RV and proper motion that differ from that of 212651234 by only $\sim$1.4 km s^{-1} and $\sim$3 mas yr^{-1}. This set of similar space velocities in three dimensions strongly implies that these two objects are also physically bound, making this at least a quintuple star system.

Key words: binaries : close – binaries: eclipsing – binaries: general – binaries: spectroscopic – binaries: visual.

1 INTRODUCTION

The *Kepler* mission, with its exquisite photometric precision (Borucki et al. 2010; Batalha et al. 2011) has revolutionized the study of stars in general, and binary stars, in particular. There were some 3000 binaries discovered in the *Kepler* main field (Slawson, Prša & Welsh 2011; Matijevič et al. 2012; Kirk et al. 2016), and there is a growing collection of binaries that have been found to date in the 2-wheel extension of the *Kepler* mission, called 'K2' (Howell

et al. 2014; LaCourse et al. 2015). Among this impressive collection of mostly eclipsing binaries, some 220 triple stars have been discovered (Rappaport et al. 2013; Conroy et al. 2014; Borkovits et al. 2015, 2016), mostly through eclipse timing variations, but some via third-body eclipses. In addition to the large sample of triple star systems, a number of higher order multiple star systems have also been discovered using *Kepler* data plus follow-up ground-based observations (quadruple 4247791: Lehmann et al. 2012; quadruple 7177553: Lehmann et al. 2016; and quintuple KIC 4150611/HD 181469: Shibahashi & Kurtz 2012, and references therein; Prša et al. in preparation). Other quintuple systems, not found with *Kepler*, include: 1SWASP J093010.78+533859.5 (Lohr et al.

* E-mail: sar@mit.edu

2015); the young B-star quintuple HD 27638 (Torres 2006); HD 155448 (Schütz et al. 2011); 14 Aurigae (Barstow et al. 2001); σ^2 Coronae Borealis (Raghavan et al. 2009); GG Tau (Di Folco et al. 2014), HIP 28790/28764 and HIP 64478 (Tokovinin 2016), and V994 Her (Zasche & Uhlař 2016). Aside from being intrinsically fascinating systems, we can learn the most about the formation and evolution of multiple star systems if the constituent stars are close enough to interact dynamically on time-scales of less than a few years.

In this work we report the first quintuple star system found in the K2 fields, and one of a relatively few that contain two eclipsing and spectroscopic binaries. This work is organized as follows. In Section 2, we present the K2 Field 6 data in which the two eclipsing binaries, 'A' and 'B', were discovered to be in the same stellar image. Our optical radial velocity (RV) studies are discussed in Section 3, and Keplerian orbits are fit to the RV data in Section 4. We evaluate the full set of parameters for the 'A' and 'B' binaries in Section 5 using a Monte Carlo evaluation process. The spectra are analysed in Section 6 to further confirm our parameter determinations for binaries 'A' and 'B'. We consider the tidal status of binaries 'A' and 'B' in Section 8. In an effort to further probe the structure of the system we obtained adaptive optics (AO) and speckle-interferometric images of the system; these are presented in Section 9. The photometric distance to the target is derived in Section 10. We discuss in Section 11 the constraints that can be set on 'binary C' which is composed of binaries 'A' and 'B' that are gravitationally bound to each other. Binary 'D' comprised of binary 'C' in orbit about the apparently single star EPIC 212651234, is discussed in Section 12. We investigate the single star EPIC 212651234 in Section 13. Finally, we summarize our results in Section 14.

2 K2 OBSERVATIONS

As part of our ongoing search for eclipsing binaries, we downloaded all available K2 extracted light curves common to Campaign Field 6 from the MAST.[1] The flux data from all 28 000 targets were high-pass filtered with a cut-on frequency of 1 d. The data files were then Fourier transformed to facilitate a search for objects with periodic signatures. The folded light curves of targets with significant peaks in their Fourier transforms were then examined by eye to look for unusual objects with periodic features. Unfolded and normalized light curves for targets lacking significant peaks in their FFTs were also examined by eye to look for aperiodic or quasi-periodic signatures.

One object that stood out was EPIC 212651213 (hereafter 'E1213') which exhibited eclipses with a 5-d period, but where the folded light curve also showed the presence of eclipses that did not fit this period. The raw light curve is shown in Fig. 1 and the two nearly equal eclipses of the 5-d orbital period are readily apparent. However, there is also another set of unequally spaced, more shallow eclipses whose locations are marked in the figure with short vertical red lines to guide the eye. These correspond to a different eclipsing eccentric binary with a 13-d period.

We also noticed that the target EPIC 212651234 (hereafter 'E1234') exhibited the same two sets of eclipses, but with reduced amplitudes. The SDSS image of the sky in the vicinity of these two targets (see Fig. 2?>) shows two comparably bright stellar images that are separated by ∼11 arcsec. The properties of these two stars are summarized in Table 1. Investigation of
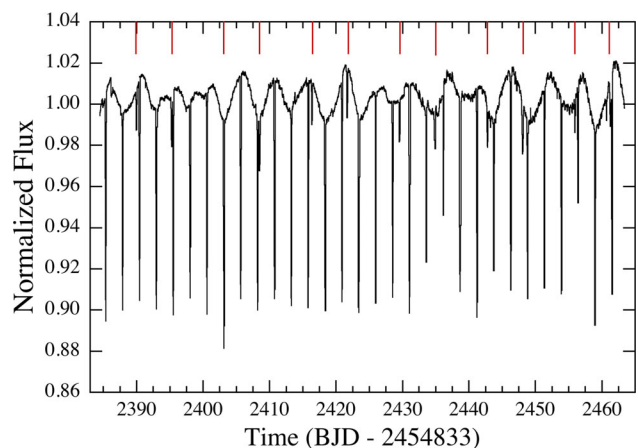
Figure 1. K2 flux data for E1213. The two eclipses of the 5-d 'A' binary are readily visible. The short red vertical lines mark the two unequally spaced eclipses of the 13-d eccentric 'B' binary.

Figure 2. SDSS image showing E1213 and E1234. The image is 7 arcmin × 7 arcmin, and shows the two images, of roughly the same magnitude, as an obviously physically related pair. In fact, the two objects have RVs and proper motions that are the same to within ∼1.7 km s^{-1} and 3 mas yr^{-1}, respectively. North is up and east is to the left.

the Target Pixel Files for E1213 and E1234 with Guest Observer software PYKE[2] (Still & Barclay 2012)[3] confirmed that the location of the photometric aperture for each of these two targets slightly overlaps the other star. By narrowing these apertures and performing a series of independent extractions on each target we were able to tentatively conclude that the source of *both* eclipsing binary signals is, in fact, E1213. (We have subsequently confirmed this with narrow-slit and fibre-fed spectroscopic observations – see Section 3.)

We present the folded light curves for each of the eclipsing binaries in Fig. 3. We used the Ames K2 PDC data, which have been

Table 1. Properties of the E1213/1234 system.

Parameter	212651213	212651234
RA (J2000)	$13^h55^m43^s.464$	$13^h55^m42^s.762$
Dec (J2000)	$-09°25'05''.92$	$-09°25'04''.02$
K_p	10.80	11.14
u^a	14.21	14.63
B^b	11.77	12.32
V^b	10.98	11.31
r'^c	11.08	11.24
J^d	9.93	9.74
H^d	9.59	9.27
K^d	9.54	9.18
$W1^e$	9.36	9.10
$W2^e$	9.40	9.21
$W3^e$	9.30	9.09
$W4^e$	8.59	8.69
Distance (pc)^f	260 ± 50	260 ± 50
V_{rad} (km s^{-1})	-13.5 ± 0.5^g	-15.0 ± 0.5
μ_α (mas yr^{-1})^h	-29.7 ± 1.3	-32.6 ± 1.9
μ_δ (mas yr^{-1})^h	-10.9 ± 1.9	-12.6 ± 1.5

^{a}Taken from the SDSS image (Ahn et al. 2012). ^{b}From APASS (https://www.aavso.org/apass). ^{c}Carlsberg Meridian Catalogue (http://svo2.cab.inta-csic.es/vocats/cmc15/). ^{d}2MASS catalogue (Skrutskie et al. 2006). ^{e}WISE point source catalogue (Cutri et al. 2013). ^{f}Based on photometric parallax only. ^{g}The mass-weighted mean of the γ velocities for the 'A' and 'B' binaries (see text). ^{h}From UCAC4 (Zacharias et al. 2013), and Huber et al. (2016).
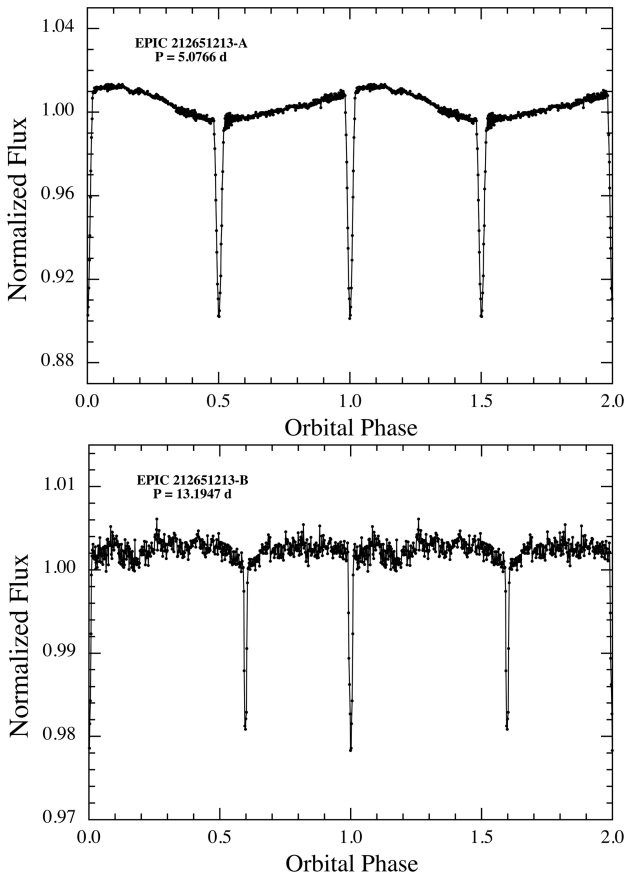
Figure 3. Folded light curves for the 5-d circular binary 'A' (top panel) and 13-d eccentric binary 'B'. These have been 'disentangled' by subtracting the folded profile of each, sequentially, from the raw flux time series shown in Fig. 1 and then refolding the data.

corrected for the dilution by the other star. In each case, we subtracted the folded light curve of the other eclipsing binary in such a way as to effectively 'clean' the data of the modulations due to the other binary. To accomplish this, the folded data used for the subtraction was produced while eliminating the phases around the other binary's eclipses.

The eclipse timing analysis, for determining orbital periods, phase zero of the eclipses, and relative eclipse separations, was carried out as described in Borkovits et al. (2015, 2016). This includes allowance for local trends in the out-of-eclipse regions near the eclipses.

The 5.077-d binary (top panel of Fig. 3), hereafter designated as 'Binary A', has two nearly equal depth eclipses that are separated by very close to half an orbital cycle. The fitted fractional separation between eclipses differs by only 325 ± 187 ppm from half an orbital cycle, and we can then utilize the approximate expression (good to second order in eccentricity e):

$$e \cos \omega_A \simeq \frac{\pi}{2} \left[\frac{1}{2} - \frac{\Delta t_{(II,I)}}{P_{orb}} \right] \qquad (1)$$

to say that $e \cos \omega_A \lesssim 0.0008$, which is indicative of a rather circular orbit unless the longitude of periastron, ω, for the binary is within $\sim 1/2°$ of 90° or 270°. In this expression $\Delta t_{(II, I)}/P_{orb}$ is the fractional time difference between the two closely spaced eclipses. We can also utilize information from the relative widths of the two eclipses, w_1 and w_2, to find a measure of $e \sin \omega$. For small e and arbitrary ω:

$$e \sin \omega \simeq \frac{(1 - w_2/w_1)}{(1 + w_2/w_1)} \qquad (2)$$

From the K2 photometry, we determine that $w_2/w_1 = 0.996 \pm 0.014$. Therefore, $e_A \sin \omega_A = 0.002 \pm 0.02$. Thus, based on the limits obtained from equations (1) and (2) we can constrain the orbital eccentricity of the 'A' binary to be

$$e_A \lesssim 0.02.$$

Finally, we note the out-of-eclipse modulation with an ~ 1 per cent amplitude that is in phase with the binary orbit, but is not due to ellipsoidal light variations (which would have minima at the eclipses), and we ascribe this modulation to star-spots on one or both stars of the 'A' binary. Fig. 3 also shows that the apparently irregular variations seen in the out-of-eclipse regions in Fig. 1 could be well modelled in this way.

In the bottom panel of Fig. 3, the 13.1947-d eccentric binary is more clearly revealed. For this set of eclipses, we find the closely spaced pair to be separated by 0.4019 (± 0.0002) orbital cycles. From equation (1), we find $e_B \cos \omega_B = 0.154$. In Section 4, we are able to compare this to the results we find by directly measuring e_B and ω_B from RV studies, and find excellent agreement.

3 RV OBSERVATIONS

We have carried out 27 RV measurements of E1213 on 25 different nights. Eight of these were carried out with the Tillinghast Reflector Echelle Spectrograph (TRES) at the Fred Lawrence Whipple Observatory (FLWO), 16 were obtained at Thüringer Landessternwarte Tautenburg (TLS), and three were acquired at the Konkoly Observatory of the Hungarian Academy of Sciences. Here we briefly describe the spectroscopic observations at each facility. In addition, we have obtained 11 spectra of E1234.

3.1 RV observations with the TLS spectrograph

Spectra of E1213 and E1234 were taken using the Coudé-Echelle Spectrograph on the 2-m Alfred Jensch Telescope at TLS. The spectrograph was used with a projected slit width of 2 arcsec providing a resolving power of $R = 30\,000$. We obtained 16 spectra of E1213 and three spectra of E1234 with 40 min of exposure time each.

Spectrum reduction was done using standard ESO-MIDAS packages and included bias and stray-light subtraction, filtering of cosmic ray events, flat fielding using a halogen lamp, optimum order subtraction, wavelength calibration using a Thorium–Argon (ThAr) lamp, normalization to the local continuum, and merging of spectral orders. Small shifts in the instrumental zero-point were removed from each spectrum using a large number of telluric O_2 lines as reference. The long-time RV accuracy reached with this spectrograph and reduction procedure depends on spectral type and $v \sin i$ of the observed star and is about $100\,\mathrm{ms^{-1}}$ for sharp-lined, solar-type SB1 stars.

3.2 RV observations with the TRES spectrograph

Spectra of E1213 and E1234 were taken using the TRES (Szentgyorgyi & Furész 2007), on the 1.5-m telescope at the FLWO on Mt Hopkins, Arizona. TRES is a fibre-fed optical spectrograph with a resolving power of $R = 44\,000$. We obtained eight spectra of E1213 between UT 2016-02-21 and UT 2016-03-23 with a typical exposure time between 660 and 1200 s, and an average signal-to-noise ratio (S/N) per resolution element of 38. E1234 was observed six times between UT 2016-02-21 and UT 2016-05-03 with the exposure time ranging between 360 and 1500 s, and an average S/N of 28. The spectra were extracted following the procedures reported by Buchhave et al. (2010).

3.3 RV observations at the Konkoly observatory

E1213 and E1234 were observed during three nights in 2016 March with the fibre-fed ACE spectrograph attached to the 1-m RCC telescope of the Konkoly Observatory at Piszkés-tető, Hungary. The instrument covers the 0.415–0.915 μm wavelength range with a resolution of $R = 20\,000$. The fibre entrance has a sky-projected diameter of ≈2.5 arcsec, which assured complete separation of the light from the two stellar images of E1213 and E1234. The light of a ThAr lamp can be projected on the entrance of the same fibre that is used for stellar observations for precise wavelength calibration.

The individual 1800-s exposures had S/N ≈ 25 pixel^{-1} around 0.55 μm. The RV measurements were averaged for 3–4 consecutive exposures, with the exception of the night 2457 466, when only one exposure of E1213 was obtained.

The spectra were reduced using IRAF[4] standard tasks including bias, dark, and flat-field corrections, aperture extraction, wavelength calibration (using ThAr exposures) and barycentric correction. The normalization, cosmic ray filtering, order merging, and cross-correlation were performed by in-house developed programs of ÁS.

The systematic errors introduced by the data processing and the stability of the wavelength calibration system were found to be better than $0.36\,\mathrm{km\,s^{-1}}$, based on RV standard observations (Derekas et al. 2016).

---

[4] IRAF is distributed by the National Optical Astronomy Observatories, which are operated by the Association of Universities for Research in Astronomy, Inc., under cooperative agreement with the National Science Foundation.

Table 2. RV measurements[a] of E1213.

BJD-2457000	Star 3	Star 1	Star 2	Observatory[b]
437.6168	+12.19	−81.16	+61.41	TLS
438.6121	−2.51	−58.44	+36.12	TLS
439.9122	−16.51	+44.81	−73.27	TRES
446.6095	−37.42	+23.19	–	TLS
448.9694	+31.19	−39.03	+31.2	TRES
449.9451	+27.26	–	−61.37	TRES
450.9174	+10.11	59.15	−82.62	TRES
451.9094	−5.34	−5	−5	TRES
452.9020	−14.53	−81.25	+63.81	TRES
454.8921	−35.03	+25.78	−35.0	TRES
465.5360	−8.09	+58.12	−86.10	KO
466.4933	−22.35	–	–	KO
470.5774	−55.28	+54.68	–	KO
470.8631	−53.91	+64.01	−84.58	TRES
474.5096	+11.98	−30.42	+24.79	TLS
475.5136	+31.89	+41.28	−78.39	TLS
480.4751	−27.17	+46.06	−71.18	TLS
481.4721	−36.86	+54.41	−80.15	TLS
481.5004	−37.39	+52.06	−78.97	TLS
482.4861	−44.79	−24.50	+3.67	TLS
493.4864	−25.89	−82.04	+64.39	TLS
497.5090	−56.17	+16.96	−0.37	TLS
498.4503	−54.82	−79.09	+53.90	TLS
499.4943	−34.01	−52.66	+40.91	TLS
502.4660	+25.08	−1.47	−26.40	TLS
502.5105	–	+24.23	−21.96	TLS
503.5078	+8.48	−72.66	+55.71	TLS

[a]Units are $\mathrm{km\,s^{-1}}$ and the typical empirical uncertainties on the RV values are $1.7\,\mathrm{km\,s^{-1}}$ for star 3 and $7\,\mathrm{km\,s^{-1}}$ for stars 1 and 2. [b] 'TLS' stands for the Thüringer Landessternwarte Tautenburg, 'KO', the Konkoly Observatory, and 'TRES' is the Tillinghast Reflector Echelle Spectrograph of the Whipple Observatory.

Table 3. RV measurements[a] of E1234.

BJD-2457000	E1234	Observatory[b]
439.9296	−14.88	TRES
446.6384	−15.63	TLS
448.9837	−14.75	TRES
452.9111	−14.73	TRES
465.6044	−14.79	KO
466.9254	−14.77	TRES
470.5024	−14.59	KO
475.5430	−15.78	TLS
476.5049	−15.53	TLS
504.8558	−14.80	TRES
511.8791	−15.01	TRES

[a]Units are $\mathrm{km\,s^{-1}}$ and the typical uncertainties on the RV values are $0.1\,\mathrm{km\,s^{-1}}$ for any one observatory. [b] 'TLS' stands for Thüringer Landessternwarte Tautenburg, 'KO', the Konkoly Observatory, and 'TRES' is the Tillinghast Reflector Echelle Spectrograph of the Whipple Observatory.

3.4 RV analysis

Summaries of the 27 RV observations of E1213 and 11 observations of E1234 are given in Tables 2 and 3. In all, the measurements of E1213 span an interval of some 66 d.

For each observation, we cross-correlated the acquired spectrum with a single reference template stellar spectrum. We utilized the template spectrum that yields the highest peak correlation value
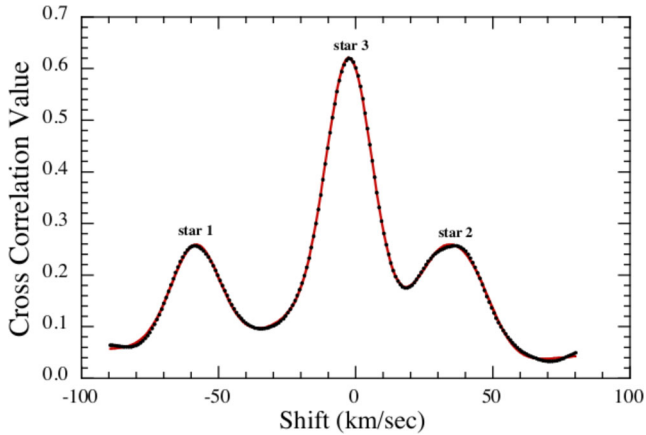
Figure 4. Illustrative cross-correlation function calculated between the observed spectrum and a stellar reference spectrum as a function of the shift in velocities. The three prominent peaks labelled as 'star 1', 'star 2', and 'star 3', mark the RVs of the three stars that can be detected in the CCF. Stars 1 and 2 comprise the A binary, while star 3 is the brighter of the two stars in the eccentric binary. The fourth star is not detected in any of the RV spectra. The red curve is a model fit to the CCF which locates the peaks quantitatively.

after testing a grid of $T_{\rm eff}$ and $\log g$ values, for an assumed solar metallicity. An illustrative cross-correlation function ('CCF') is shown in Fig. 4. The reference spectrum was for $T_{\rm eff} = 5900$ K and $\log g = 4.2$, close to values ultimately derived for star 3. The three clearly discernible peaks correspond to three stars in the two binaries that are detectable in these RV studies. The RVs were measured by modelling the CCFs using two profiles with common centres, one Gaussian plus one Cauchy, per stellar component. When the peaks are clearly separable, as in the example in Fig. 4, the RVs of these three stars can be well measured. When the peaks are closer, or even merged, we may be able to determine only the RV of star 3 which dominates the CCF in all observations. Lines of star 4 could not be detected in any of the spectra. In particular, we checked when stars 1 and 2 have very small RVs, and simultaneously the RV of star 3 is large – star 4 is still not detected in the CCFs, even with a lower temperature reference spectrum. The measured RVs for the three detectable stars in E1213 are summarized in Table 2.

We also obtained 11 spectra for E1234. Only a single peak in the CCF is measured in any of these. The 11 RVs for this image are reported in Table 3. We interpret this in terms of either a single star within E1234 or perhaps a binary with an orbit that is sufficiently wide that no RV changes are detected. We can set a limit of $\lesssim 0.5$ km s^{-1} for RV variations over the 72-d interval of the observations (for more stringent constraints, see Section 13).

The RV points for the circular binary, folded modulo the 5-d period are shown in the top panel in Fig. 5, while those for the 13-d binary are plotted in the bottom panel of Fig. 5.

4 RV ORBITS

4.1 Fitting the 'A' binary

Given the very small value of $e \lesssim 0.02$ for the 'A' binary that we were able to deduce from the K2 light curve (see Section 2), we restricted our fits to circular orbits. We fit the RV points shown in the upper panel of Fig. 5 simultaneously for the orbits of stars 1 and 2 using common values of the orbital phase and γ_A velocity, as well as K_1 and K_2 velocities. We fixed the orbital period at $P_{\rm orb}$
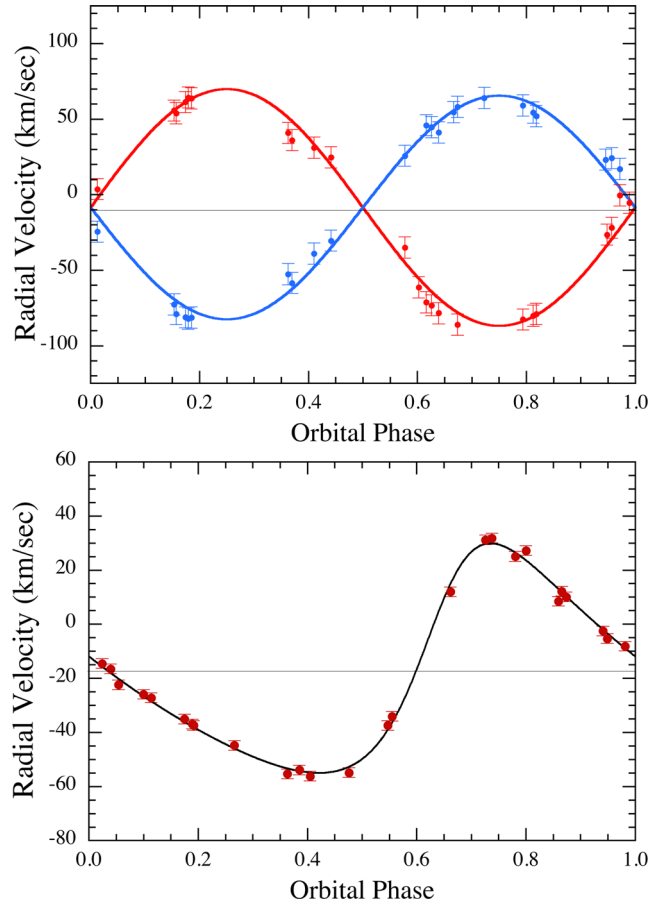
Figure 5. RV curves for the 'A' binary (top panel) and the 'B' binary (bottom panel). The solid curves are the best-fitting solutions. For the 'A' binary the fitted parameters are the two K velocities, γ_A, and orbital phase. (Blue and red curves are the primary and second star, respectively.) The orbital period was fixed at the value of 5.0766 d as determined from the K2 photometry. For the 'B' binary the fitted parameters are: K_3, e_B, τ_B, ω_B, and γ_B (see Section 4 for details.) Note that we have chosen here to define orbital 'phase' zero as the time of primary eclipse.

$= 5.0766$ d, as determined from the K2 data. This is more accurate than the period we would be able to determine from the RV data alone. We utilized a simple Levenberg–Marquardt fitting routine to determine the four unknown parameters (K_1, K_2, γ_A, $t_{0,\rm RV}$) and their uncertainties.

The best-fitting model RV curves for the 'A' binary are shown in the top panel in Fig. 5, and the fitted orbital parameters are summarized in Table 4. The values of K_1 and K_2 are 73.5 and 78.1 km s^{-1}, respectively; these are similar but do differ at the 1.6σ level. The orbital phase agrees with the phase obtained from the K2 photometry and projected forward by nearly half a year. The agreement is good to within 0.047 d with an uncertainty of 0.025 d (i.e. $\sim 1.1 \pm 0.6$ h).

We also note that star 1, with the somewhat lower K velocity (compared to star 2), and hence the higher mass, is the one whose descending node on the RV curve is an integer number of orbital cycles from the slightly deeper eclipse in the K2 light curve (see the top panel of Fig. 3). This is the time when the more massive star is eclipsed. And, at least for stars on the main sequence, the more massive star should have the higher surface brightness, and hence the deeper eclipse when it is transited – just as we observe.

We use the K values to derive the constituent masses in Section 5.

Table 4. Properties of the 'A' binary[a].

Parameter	Star 1	Star 2
P_{orb} (d)[b]	5.07655 ± 0.00003	5.07655 ± 0.00003
K (km s^{-1})[c]	73.5 ± 2.0	78.1 ± 2.1
δK_{rms} (km s^{-1})[c]	6.9	6.9
a (R$_\odot$)[c]	7.38 ± 0.20	7.84 ± 0.21
$e \cos \omega$[b]	$\lesssim 0.0008$	$\lesssim 0.0008$
$e \sin \omega$[b]	$\lesssim 0.02$	$\lesssim 0.02$
e[c]	$\lesssim 0.02$	$\lesssim 0.02$
$t_{0,RV}$ (d)[c]	436.683 ± 0.025	439.221 ± 0.025
$t_{0,K2,+35P}$ (d)[b]	436.634 ± 0.001	439.172 ± 0.001
$t_{0,K2}$ (d)[b]	258.9552 ± 0.0002	261.4935 ± 0.0002
γ_A (km s^{-1})[c]	-8.4 ± 1.0	-8.4 ± 1.0
$\dot{\gamma}_A$ (cm s^{-2})[c]	<0.01	<0.01
$f(M_1)$ (M$_\odot$)[d]	0.210 ± 0.017	0.252 ± 0.020
i_A[e]	$87°.3 \pm 0°.4$	$87°.3 \pm 0°.4$
M (M$_\odot$)[f]	0.94 ± 0.06	0.89 ± 0.05
R (R$_\odot$)[g]	0.86 ± 0.12	0.80 ± 0.09
T_{eff} (K)[g]	5475 ± 200	5250 ± 200
$\log g$ (cgs)[g]	4.54 ± 0.10	4.59 ± 0.07

[a]All values are cited with 1σ uncertainties; times are BJD-2457000. [b]Based on the K2 photometry. [c]From fits to the RV data given in Table 2, with eccentricity fixed at $e = 0$. [d]Mass function for each star based on their respective K velocities. [e]See Section 7. [f]From a Monte Carlo analysis of the system parameters and error propagation (see Section 5). [g]The extra constraints needed to yield the full set of system parameters were obtained from observational restrictions on the light ratio between the 'A' and 'B' binaries, and the Yonsei–Yale evolution tracks (see Section 5).

4.2 Fitting the 'B' binary

We next fit the RV points plotted in the bottom panel of Fig. 5 for the obviously eccentric orbit. We held the orbital period fixed at 13.1947 d, as determined from the K2 photometry, and fit for five free parameters: $a_3 \sin i_B, e_B, \omega_B, \tau_B$, and γ_B, where ω_B and τ_B are the longitude and passage time of periastron. For this, we utilized a Markov chain Monte Carlo code to map out the uncertainties in the parameters. The results are reported in Table 5. In spite of the fact that this is a single-line spectroscopic binary, we were still able to make useful mass estimates of both star 3 and star 4 via their combined flux compared to the flux from binary 'A' (see Section 5).

5 EVALUATION OF BASIC STELLAR AND ATMOSPHERIC PARAMETERS

We now have two independent mass functions for star 1 and star 2 in the 'A' binary, and a mass function for star 3 in the 'B' binary. For both binaries, the orbital inclination angles are found to be very close to 87° (see Section 7). To determine the masses and other stellar properties we utilize two ingredients: (i) the three mass functions and their uncertainties (Tables 4 and 5), and (ii) the relative fluxes of the 'A' and 'B' binaries (see e.g. Section 9.2). For the latter constraint, we adopt the following specific equality involving the stellar luminosities:

$$\frac{(L_3 + L_4)}{(L_1 + L_2)} = 1.6 \pm 0.16 (1\sigma). \tag{3}$$

We then use a Monte Carlo error propagation technique to evaluate all four masses simultaneously. First, we choose realizations for stars 1 and 2, using the cited values for the orbital K velocities and random Gaussian draws of their cited uncertainties (Tables 4 and 5). This then determines M_1 and M_2 for that particular realization

Table 5. Properties of the 'B' binary[a].

Parameter	Value
P_{orb} (d)[b]	13.1947 ± 0.0004
K_3 (km s^{-1})[c]	42.57 ± 0.28
δK_{rms} (km s^{-1})[c]	1.77
a_3 (R$_\odot$)[c]	10.51 ± 0.07
e[c]	0.325 ± 0.006
ω_B (deg)[c]	298.7 ± 1.2
τ_B (d)[c]	434.73 ± 0.05
$t_{ecl, RV}$ (d)[c]	439.45 ± 0.05
$t_{ecl, K2+16P}$ (d)[b]	439.39 ± 0.01
$t_{ecl, K2}$ (d)[b]	228.270 ± 0.003
γ_B (km s^{-1})[c]	-19.0 ± 0.2
$|\dot{\gamma}_B|$ (cm s^{-2})[c]	<0.007
$f(M_3)$ (M$_\odot$)[d]	0.089 ± 0.002
i_B[e]	$87°.6 \pm 0°.2$
M_3 (M$_\odot$)[f]	1.09 ± 0.07
M_4 (M$_\odot$)[f]	0.64 ± 0.03
R_3 (R$_\odot$)[f]	$1.07^{+0.17}_{-0.11}$
R_4 (R$_\odot$)[f]	0.57 ± 0.03
$T_{eff, 3}$ (K)[f]	6000 ± 280
$T_{eff, 4}$ (K)[f]	4280 ± 110
$\log g_3$ (cgs)[f]	$4.43^{+0.10}_{-0.16}$
$\log g_4$ (cgs)[f]	4.75 ± 0.03

[a]All values are cited with 1σ uncertainties; times are BJD-2457000. [b]Based on the K2 photometry. [c]From fits to the RV data given in Table 2. [d]Mass function based on the K velocity and the orbital eccentricity. [e]See Section 7. [f]The extra constraints needed to yield the full set of system parameters were obtained from observational restrictions on the light ratio between the 'A' and 'B' binaries, and the Yonsei–Yale evolution tracks (see Section 5).

of K_1 and K_2. Next, we similarly chose a random realization of the value of K_3 using its error bar. We then choose a random mass ratio for M_4/M_3 between 0 and 1; that, plus the mass function for star 3, yields a specific realization for M_3 and M_4.

In order to further constrain the system parameters, we require at least one more substantive constraint on the system. We take this supplemental information to be the measured ratio of the brightness of binary 'B' to binary 'A' (see Section 9). However, in order to incorporate the luminosities of the star, we need to make use of basic evolution tracks for low-mass stars. In order to do that, we have devised non-physical fitting functions to the Yonsei–Yale evolution tracks (see Fig. 6; Yi et al. 2001). The following represent the radius and luminosity evolution of a star of mass m and evolution age, t.

$$R(m, t) \simeq 0.84 \, m \, e^{m^{3.5}t/26} \left[1 + e^{(t-12.5\,m^{-3.5})/0.9} \right] \tag{4}$$

$$L(m, t) \simeq 0.66 \, m^{4.6} \, e^{m^{3.5}t/12.3} \left[1 + e^{(t-12.5\,m^{-3.5})/0.7} \right], \tag{5}$$

where m is in solar masses, and the evolution age, t, is expressed in Gyr. These should be sufficiently accurate for stars of mass $0.8 \lesssim m \lesssim 1.4$.

Thus, our Monte Carlo realizations of the system also require an evolutionary age, which we take to be uniformly distributed between 1 and 10 Gyr. Once we have a set of 4 masses and a randomly chosen evolution age, we can use equations (4) and (5) to evaluate all the system parameters, including masses, radii, luminosities, and values of $\log g$. The ratio of $(L_3 + L_4)/(L_1 + L_2)$ is then computed
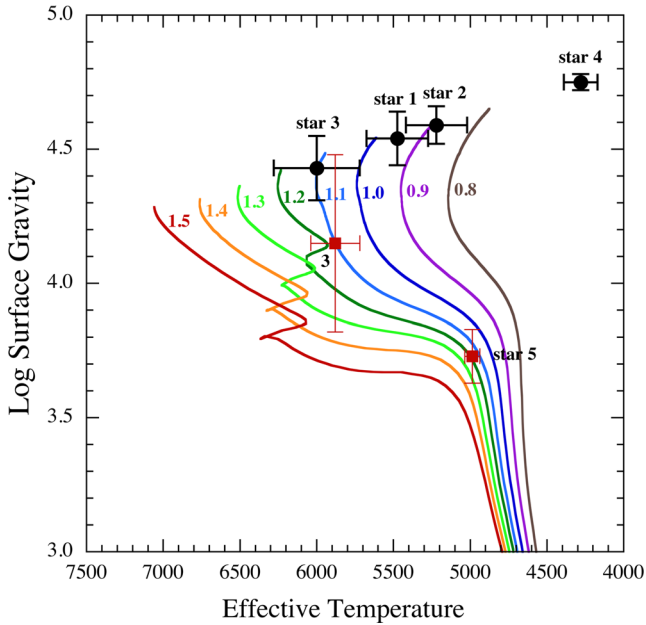
Figure 6. Evolution tracks for stars of mass 0.8 to 1.5 M$_\odot$ in the log g − T_{eff} plane. These were computed from the Yonsei–Yale tracks (Yi et al. 2001) for $Z = 0.02$. The black circles with error bars are the locations of stars 3, 1, 2, and 4 from left to right, respectively, as determined from our Monte Carlo analysis of the system parameters (see Section 5). The red error bars for star 3 show for comparison its location based on the spectrum analysis (see Section 6). Stars 1 and 2 comprise binary 'A', stars 3 and 4 are in binary 'B', while star 5 is the E1234 image. The location of star 5 is determined entirely from the spectral analysis study and is also plotted in red (see Section 6).

for the given realization. This ratio is then checked against the measured ratio given in equation (3) with a randomly chosen value with respect to the uncertainty given in that equation. If the computed ratio lies outside that of the 'measurement', the entire system is discarded.

This process is repeated 10^8 times, and distributions for the four masses, radii, T_{eff}'s, and log g's are built up. The results are shown in Fig. 7. A perusal of these mass distributions reveals a few interesting things. For the 'A' binary, the masses of stars 1 and 2 are: 0.94 ± 0.06 M$_\odot$ and 0.89 ± 0.05 M$_\odot$, respectively. The most probable values of log g are 4.54 and 4.59, with an uncertainty of 0.1 dex, respectively. The locations of stars 1 and 2 in the log g − T_{eff} plane are shown in Fig. 6, and they are clearly in good accord with the corresponding mass of the tracks they are near.

As for the 'B' binary, the mass distributions for star 3 and star 4 (see Fig. 7) indicate $M_3 \simeq 1.09 \pm 0.07$ and $M_4 \simeq 0.64 \pm 0.03$. These are rather well defined given that this is a single-line spectroscopic binary, and result from the luminosity comparison of binary 'B' with binary 'A'. The most probable values for log g are $4.43^{+0.10}_{-0.16}$ and 4.75 ± 0.03, respectively. The locations of these stars comprising binary 'B' are shown in the log g − T_{eff} plane in Fig. 6. Star 3 appears to be slightly evolved.

6 SPECTRAL ANALYSIS

The TLS spectra were taken during grey time and some of them are slightly contaminated with moonlight. Though this contamination could be separated from the stellar features in most of the CCFs used for the RV determination, we had to be sure that the contamination from the moonlight does not enter the spectrum analysis. We

therefore initially used only nine of the 16 TLS spectra of E1213 listed in Table 2 for the analysis. This number was too small for a secure decomposition of the observed composite spectra into the spectra of the individual stellar components. None the less, we tried the FFT-based KOREL program (Hadrava 1995, 2004) that delivers the orbital parameters together with the RVs and the decomposed spectra, and then the singular value decomposition of Simon & Sturm (1994) with the measured RVs as input values using the CRES code (Ilijic 2004). However, in both cases, the subsequent analysis of the decomposed spectra gave inconsistent results. In the end, we decided to analyse only the one composite spectrum that shows the largest separation of the components' peaks in the CCF (Fig. 4).

Spectrum analysis was performed using the GSSP program (see Lehmann et al. 2011 and Tkachenko et al. 2012 for a description of the method). The program is based on the spectrum synthesis approach. We extended the method to a simultaneous fit for three components in a composite spectrum. The synthetic spectra were computed on the TLS cluster computer with the parallelized version of the SYNTHV program (Tsymbal 1996), using a library of pre-computed line-by-line model atmospheres (Shulyak et al. 2004). The atomic data were taken from the VALD data base (Kupka et al. 1999). We used three grids of atmospheric parameters, one for each stellar component. Free parameters were [M/H], T_{eff}, log g, microturbulent velocity v_{turb}, and $v\sin i$. For the surface metallicities [M/H] we used scaled solar abundances in accordance with Asplund et al. (2009). Moreover, we did a fine adjustment for the RVs of the contributions of the three components, using the values obtained from fitting the CCF of the spectrum (Section 3.4) as the starting values. Normally, when we deal with an SB3 star, the flux ratios of the three stars compared to the total continuum flux are coupled via $f_1 + f_2 + f_3 = 1$ and can be determined for each grid point from least squares minimization of two of the flux ratios. In our case, we got a much better fit to the observed composite spectrum (see Fig. 8 with the fit of the Mg I triplet) when adding an additional continuum contribution (veiling), originating from star 4. In that case, f_4 is determined from $1 − (f_1 + f_2 + f_3)$ and f_1 to f_3 are no longer coupled via their flux ratios and were treated as free parameters of the fit.

We used all five of the above-mentioned quantities as free parameters for star 3. The relatively low S/N of ∼32 for the single spectrum, together with the low-line strengths of stars 1 and 2 compared to star 3, did not allow us to do the same for stars 1 and 2. For these, we fixed log g at 4.5 and 4.6, respectively, as the most probable values obtained in Section 5, and [M/H] at the value obtained for star 3 (the latter was done iteratively). After the final optimal solution for all free parameters was found, the parameter errors were determined from χ^2 statistics using the full grid of atmospheric parameters. In this way, the errors include all interdependences among the parameters.

A comparison of log g and T_{eff} for star 3 derived from this spectrum analysis (Table 6) with those inferred from the Monte Carlo evaluation of the system parameters (see Section 5) is shown in Fig. 6. The values of log g differ by 0.28 dex between that found from the spectrum analysis versus that from the MC analysis. While this difference is only about 1σ, it is none the less suggestive that star 3 may be somewhat more evolved than the MC analysis indicates. The inferred values of the flux ratio of binary 'B' to binary 'A' from the spectrum analysis is 2.03 ± 0.45 which is consistent with the value of 1.58 ± 0.16 derived from the speckle imaging (see Section 9.2). Overall, we take the spectrum analysis to be a satisfactory check on our more detailed parameter study in Section 5.
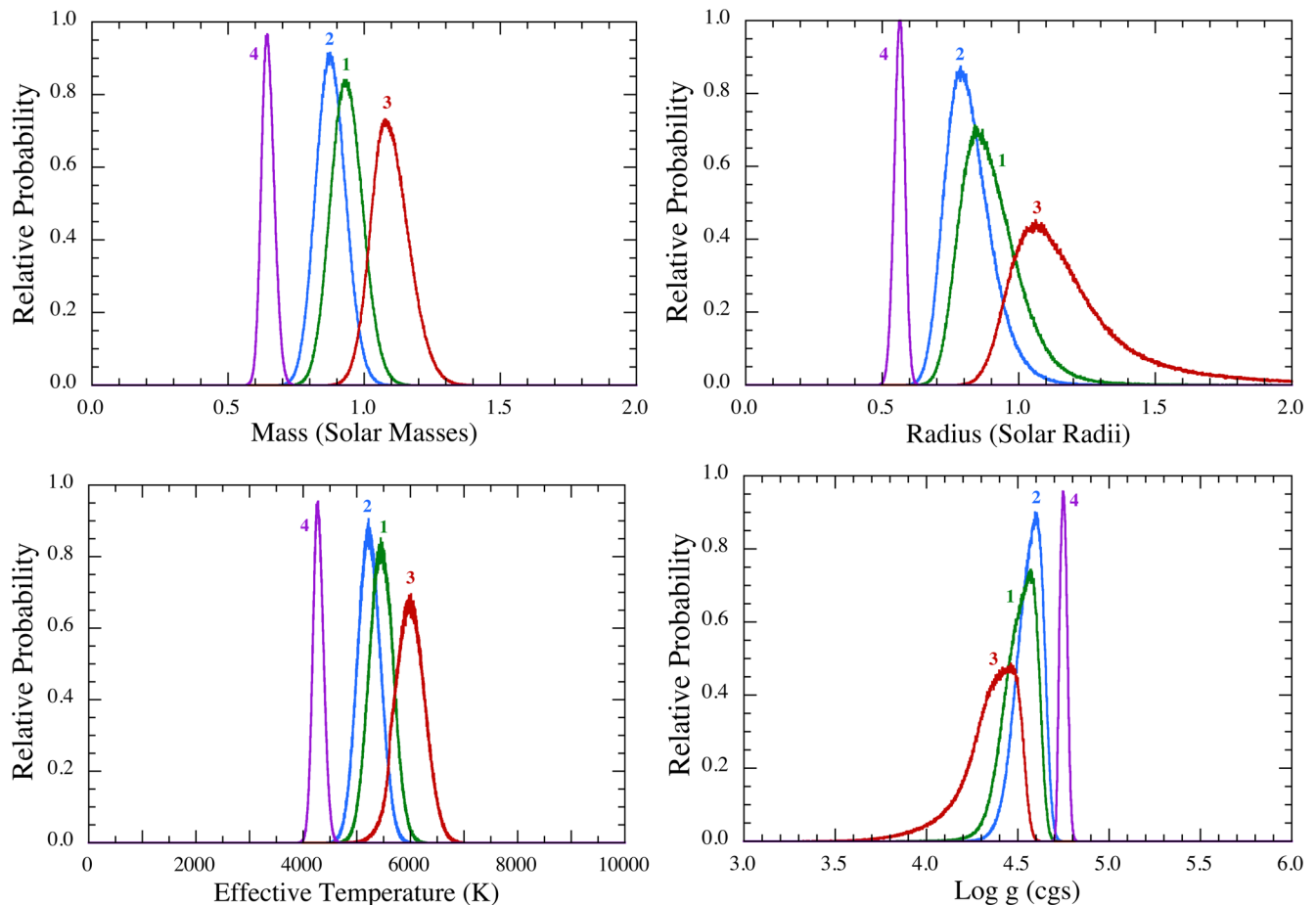
Figure 7. Probability distributions for the masses, radii, effective temperatures, and values of log *g* of the four stars in binaries 'A' and 'B'. These were computed from a Monte Carlo error propagation code using the uncertainties in the three *K* velocities. To close the equations, we also added the constraint from the speckle images (see Section 9.2) that the luminosity of binary 'B' exceeds that of binary 'A' by a factor of 1.6 ± 0.16 (see equation 3).
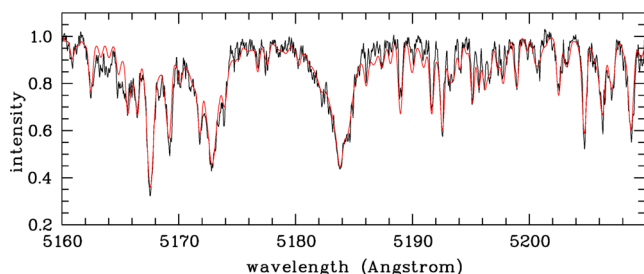
Figure 8. Part of the analysed composite spectrum of E1213 (black colour) showing the Mg I triplet region, together with the best-fitting combination of synthetic spectra (red colour; see Table 6, stars 1 to 3).

Table 6. Results from spectrum analysis.

Parameter	Star 1	Star 2	Star 3	Star 5[a]
$T_{\rm eff}$ (K)	5700 ± 250	5490 ± 310	5880 ± 160	4987 ± 50
log *g* (cgs)	$\{4.5\}^{b}$	$\{4.6\}^{b}$	4.15 ± 0.33	3.73 ± 0.1
[*M*/H]	$\{0.1\}^{b}$	$\{0.1\}^{b}$	0.08 ± 0.20	0.34 ± 0.08
$v_{\rm turb}$ (km s^{-1})	1.6 ± 0.6	1.7 ± 0.7	1.6 ± 0.4	$\{1.0\}^{b}$
$v_{\sin i}$ (km s^{-1})	13 ± 5	7 ± 6	14 ± 1.8	2.7 ± 0.5
f^{c}	0.20 ± 0.05	0.13 ± 0.04	0.59 ± 0.05	–

[a] Star 5 refers to the image of E1234. [b] Quantities in curly brackets were held fixed at plausible representative values. [c] Fraction of the light in stars 1–4.

Finally, we obtained the stellar parameters for E1234 using the Spectral Parameter Classification (SPC) tool developed by Buchhave et al. (2012). SPC cross-correlates an observed spectrum against a grid of synthetic spectra based on Kurucz atmospheric models (Kurucz 1992). The weighted average for the six TRES spectra of E1234 is $T_{\rm eff} = 4987 \pm 50$ K, log $g = 3.73 \pm 0.10$, [m/H] $= 0.34 \pm 0.08$, $v \sin i = 2.7 \pm 0.5$ km s^{-1}. The values were calculated by taking an average of the stellar parameters that were calculated for each spectrum individually. The values are then weighed according to the cross-correlation function peak height.

Table 6 summarizes the spectral analysis results for both E1213 and E1234, while Fig. 6 shows where the different stars fall in the log $g - T_{\rm eff}$ plane.

7 ORBITAL INCLINATION ANGLES

It is clear that the orbital inclination angles of both binaries are fairly close to 90° given that both exhibit eclipses with typical orbital separations of 15 and 28 R$_\odot$ for binaries 'A' and 'B', respectively, and all stars have radii $\lesssim 1.1$ R$_\odot$. We were therefore able to find the masses, radii, luminosities, etc. where the additional uncertainty due the lack of detailed knowledge of *i* added at most 0.5 per cent uncertainty (added in quadrature) which is negligible in comparison with the overall uncertainties on these parameters (see Section 5). Once we know the various system parameters we can go back and utilize the eclipse depths seen in Fig. 3 to estimate rather accurate

Table 7. Light ratios of 'A' to 'B'.

Waveband	Δ Magnitude ('A'–'B')
0.692 μm	0.55 ± 0.1^a
0.880 μm	0.45 ± 0.1^a
J	0.48 ± 0.01^b
Ks	0.64 ± 0.03^b

[a]Based on the speckle images (see Section 9.2).
[b]Based on the Keck AO imaging (see Section 9.1).

values of orbital inclination angle. The observed eclipse depths are: 11.5 and 9.2 per cent for the primary and secondary eclipses in binary 'A', and 2.2 and 1.9 per cent for the eclipses in binary 'B'.

In order to evaluate the inclination angles implied by these eclipse depths, we utilized a simple geometrical model wherein each star is taken to be a limb-darkened sphere (given the large orbital separations). Limb-darkening corrections were made using a quadratic limb-darkening law, with coefficients taken from Claret & Bloemen (2011) for the *Kepler* bandpass and for stars of the appropriate $T_{\rm eff}$ and $\log g$. We also take into account bolometric corrections to *Kepler's* band pass. We then used a related version of our Monte Carlo error propagation code (see Section 5) to allow for all the system uncertainties to be used in the calculation of the eclipse depths. The contribution of the third light to each binary is just a bit uncertain because of the disentanglement of the binary 'A' and binary 'B' light curves, and to a much lesser degree by light from E1234 leaking into the photometric aperture of E1213. In our analysis, we allow for a generous uncertainty in the third-light contributions over the range 30–60 per cent in binary 'A' and 20–40 per cent in binary 'B' (see Table 7). Starting with a uniform prior on orbital tilt angles, evaluations of the eclipse depths are run many times until a probability distribution for the inclination angles is built up.

The somewhat less well-constrained orbital inclination angle is for binary 'A' where we find $i_A = 87°.3 \pm 0°.4$. By contrast, the primary eclipse of binary 'B' is more tightly constraining and yields: $i_B \simeq 87°.6 \pm 0°.2$. The reason is that for such grazing eclipses even slightly lower values of i_B would produce primary eclipse depths that are much larger than observed, while for slightly larger values of i_B the primary eclipse would be lost altogether. At the orbital phase where the primary eclipse occurs, the orbital separation is close to 35 $R_\odot$. The sum of the two stellar radii is only $\simeq 1.65 R_\odot$. Therefore there is a critical angle of $\approx 87°$ below which there would be no eclipses.

The fact that $i_B \simeq i_A$ to within $\sim 0°.3$ does not 'prove' that the mutual inclination angle between the two orbital planes is close to zero, but any other mutual inclination angle becomes rapidly more implausible for larger and larger assumed values. By contrast there is nothing to suggest that the outer orbit between 'A' and 'B' is, or is not, aligned with the binary planes. It is quite possible that the latter angle is locked near 40° due to the Kozai–Lidov cycle with tidal friction (Lidov 1962; Kozai 1962; Kiseleva et al. 1998; Fabrycky & Tremaine 2007). This latter statement is not at odds with the fact that the orbital inclination angle of the outer binary is $\gtrsim 50°$ (Section 11).

8 TIDAL SYNCHRONIZATION STATUS OF 'A' AND 'B'

The spectroscopically obtained projected rotational velocities of stars 1–3 (see Table 6) carry indirect information on the state of the tidal synchronization processes in the two eclipsing binaries.

The projected synchronized (or, in the case of an eccentric system: pseudo-synchronized) rotational velocity of the binary members can be calculated simply as

$$(v_{\rm star} \sin i_{\rm orb})_{\rm sync} = \frac{2\pi R_{\rm star} \sin i_{\rm orb}}{P_{\rm orb} \mathcal{P}(e)}, \tag{6}$$

where $\mathcal{P}(e)$ the orbital eccentricity-dependent ratio of the orbital to the (pseudo-)synchronized rotational period which, in the equilibrium tide model of Hut (1981) can be calculated as

$$\mathcal{P}(e) = \frac{(1-e^2)^{3/2} \left(1 + 3e^2 + \frac{3}{8}e^4\right)}{1 + \frac{15}{2}e^2 + \frac{45}{8}e^4 + \frac{5}{16}e^6} < 1. \tag{7}$$

Furthermore, we also assumed that for (pseudo-)synchronized rotation the orbital angular momentum vectors of the star and orbit are aligned. Substituting stellar radii, orbital inclinations, periods, and eccentricities from Tables 4 and 5 we arrive at $(v_{\rm star}\sin i)_{\rm obs}/(v_{\rm star}\sin i)_{\rm sync} = 1.5 \pm 0.6$, 0.9 ± 0.8, and 2.1 ± 0.4 for stars 1, 2, and 3, respectively. Therefore, we can conclude that the stars in the 5-d circularized binary 'A', are rotationally synchronized with a significant likelihood. (Although, theoretically, we cannot exclude the possibility of faster stellar rotations around misaligned rotational axes.) For the primary star of the eccentric binary 'B', our result strongly supports a modestly supersynchronous rotation.

According to the formulae of Moreno, Koenigsberger & Harrington (2011) and Zahn (2008), for a convective star in an eccentric $e \sim 0.3$ orbit with a fractional radius of $R_{\rm star}/a \sim 0.04$, the expected synchronization time-scale even for an initially 10 times faster orbital rotation should be $\lesssim 1$ Gyr for physically realistic values of the viscosity parameter. This time-scale is shorter than the likely age we infer for the system. Therefore, we might expect some secondary source working against synchronized rotation, which might be indirect evidence for dynamical perturbations of binary 'A' on binary 'B'.

9 HIGH-RESOLUTION IMAGING

9.1 Keck AO

To obtain better constraints on this quintuple system, we imaged both E1213 and E1234 on 2016 April 13 UT with the NIRC2 instrument (PI: Keith Matthews) on Keck II using natural guide star imaging with the narrow camera setting (10 milliarcseconds, 'mas', pixel^{-1}). We used a three-point dither pattern to avoid NIRC2's noisier lower-left quadrant and we calibrated the images and removed artefacts using dome flat-fields and dark images.

We obtained 12 images of E1213 in the K_s band (central wavelength 2.145 μm) for a total on-sky integration time of 300 s. Fig. 9 (top panel) shows a stacked image of this target, in which we see two peaks. For each calibrated frame, we fit a two-peak PSF to measure the flux ratio and on-sky separation. We model the PSF as a combined Moffat and Gaussian shape. The best-fitting PSF was found over a circular area with a radius of 10 pixels around each star (the full width at half-maximum of the PSF was about 5 pixels). More details of the method can be found in Ngo et al. (2015). When computing the separation and position angle, we applied the new astrometric corrections from Service et al. (2016) to account for the NIRC2 array's distortion and rotation. We find the ΔK_s for binary 'A'–binary 'B' to be 0.64 ± 0.03, the separation to be 90.5 ± 1.4 mas, and the position angle of 'A' relative to 'B' to be 68.5 ± 0.9 deg E of N. We also took six images in J band (central wavelength 1.248 μm). We find the ΔJ for binary 'A'–binary 'B' to be
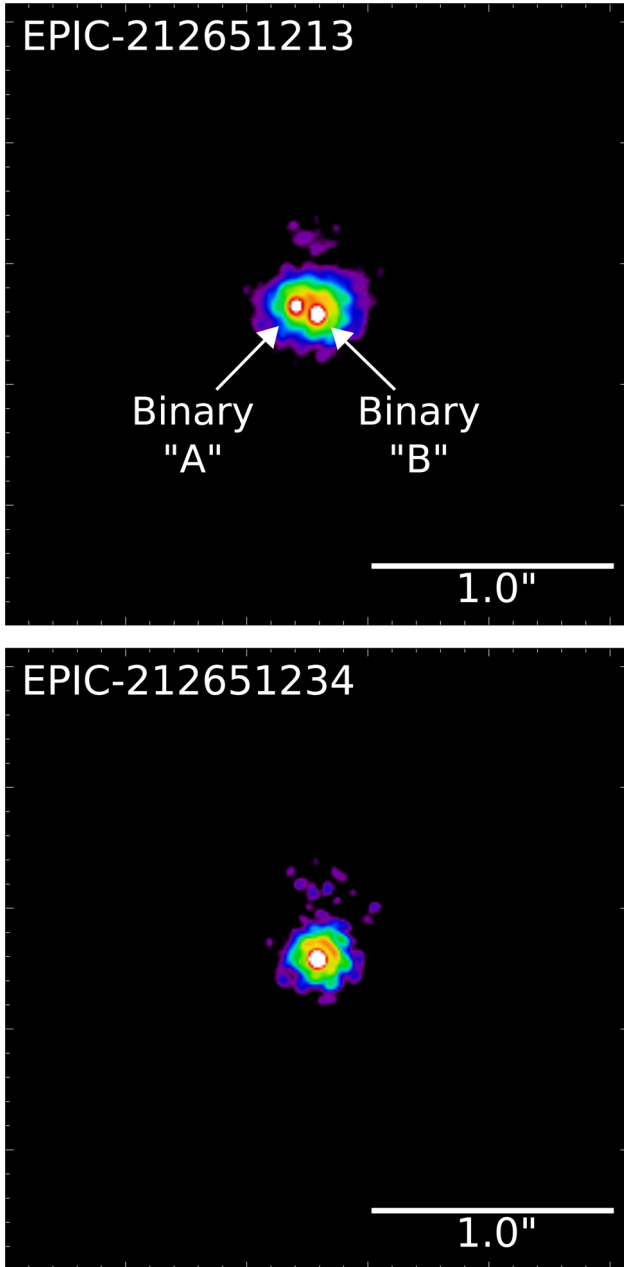
Figure 9. Top panel: Keck-AO image in K_s band of E1213. This target clearly has two cores separated by ∼0.095 arcsec. From this, we conclude that the separation between binaries 'A' and 'B' is ≈25 ± 5 au. Bottom panel: star E1234 is unresolved at the ∼0.05 arcsec level for stars of comparable magnitude.

0.48 ± 0.01. The magnitude differences between the 'A' and 'B' binaries are summarized in Table 7.

We also imaged E1234 with the same setup parameters and show the stacked image in the bottom panel of Fig. 9. We do not see more than one light source, so we compute a 5σ contrast curve to put an upper limit on an unseen companion. To determine our limiting contrast over a range of distances, we divide the stacked image into a series of annuli centred on the star with a width of 5 pixels. Then, for every pixel in each annuli, we compute the sum of all neighbouring pixels in a 5 × 5 box. The standard deviation of these values determines the 1σ contrast for that separation. The limiting magnitude is determined by dividing each limiting contrast by the flux in a 5 × 5 box centred on the primary star. At separations of 0.05, 0.10, 0.15, 0.20, and 0.5 arcsec from E1234, we rule out additional companions brighter than $\Delta K_s \simeq 0, 1.4, 2.8, 3.9,$ and 6 mag, respectively.

9.2 Speckle interferometry

We performed speckle interferometric observations at the 3.5-m WIYN telescope located on Kitt Peak using the Differential Speckle Survey Instrument (see Horch et al. 2009, 2011). This speckle camera provides simultaneous observations in two filters by employing a dichroic beam splitter and two identical electron-multiplying CCDs as the imagers. We observed E1213 and E1234 on 2016 April 17 ᵁᵀ obtaining five sets of 1000, 40-ms images for each star. The observations were performed simultaneously in narrow 'R' and 'I' bandpasses, where 'R' and 'I' have central wavelengths of 0.692 and 0.880 μm, respectively, and the corresponding FWHMs are 0.04 and 0.05 μm. Our final reconstructed images and results of the observations were obtained using the full combined data set. The details of how we obtain, reduce, and analyse the speckle interferometric results are described in Howell et al. (2011).

The speckle imaging also resolves the image of E1213 into two images that we associate with binaries 'A' and 'B' just as we found from the AO imaging (see Section 9.2). The separation on the sky in the speckle image confirms the angular separation at 90.7 mas ± 1.5 mas found in the Keck AO image. The position angle of 68°.8 agrees with that determined with the Keck AO to within the speckle uncertainty of 1°.3. We use the speckle images to determine the ratio of the fluxes from binary 'B' to binary 'A', and find 1.66 ± 0.16 at 0.69 μm, and 1.51 ± 0.15 at 0.88 μm. These ratios are summarized in Table 7. When combined with the three mass functions that we measure for binaries 'A' and 'B', these flux ratios play an important role in determining the properties of the four stars (see Section 5).

10 PHOTOMETRIC DISTANCE ESTIMATE

We can estimate the distance to E1213 and E1234 from photometric parallax. For E1213, comprised of binaries 'A' and 'B', we have good estimates of the masses, and evolutionary states of the four constituent stars, and hence their combined luminosities. We estimate that stars 1 through 4 have a combined bolometric luminosity of $L_{tot} \simeq 2.5 \pm 0.8\,L_\odot$. Since the three stars that dominate the luminosity budget are not far from solar-type stars, we take this ensemble of stars to be 1.0 ± 0.3 visual magnitudes brighter than the Sun (i.e. no significant bolometric correction), and thus it has $M_V \simeq 3.7 \pm 0.3$. The visual magnitude of E1213 is $V \simeq 10.8$, and therefore the distance modulus to the source is 7.1 mag. Finally, this leads to a distance estimate of 260 pc. When done within our Monte Carlo parameter estimation code (see Section 5), we find $d = 260 \pm 50$ pc.

For the stellar image E1234, we estimate that this apparently single star has $T_{eff} \simeq 4987 \pm 50$ K and $\log g \simeq 3.73 \pm 0.1$ (see Table 6). Its location is superposed on evolution tracks in the $\log g - T_{eff}$ plane in Fig. 6, and one can readily see that it is substantially evolved. From the location of E1234 in the H-R diagram, and the use of the Yonsei–Yale evolution tracks (Yi et al. 2001), we estimate that its bolometric luminosity is $3.4 \pm 0.9\,L_\odot$, for stars between 1.0 and 1.3 M$_\odot$. The apparent magnitude for this star is $V \simeq 11.1$, which roughly translates to $m_{bol} \simeq 10.9$. The distance modulus then comes out to be 7.5 ± 0.3, corresponding to a distance of

Table 8. Inferences about the 'C' binary.

Parameter	Binary A	Binary B
γ (km s^{-1})^a	-8.4 ± 1.0	-19.0 ± 0.2
K (km s^{-1})^b	$\simeq 5.2$	$\simeq 5.5$
$\|\dot{\gamma}\|$ (cm s^{-2})	<0.01	<0.006
θ_{AB} (arcsec)^c	0.095	0.095
P_{AB} (yr)^d	65 ± 20	65 ± 20
a_{AB} (au)^d	25 ± 5	25 ± 5

^{a}Taken from Tables 4 and 5. ^{b}We apportioned the difference in γ velocities inversely proportional to the masses of binary A (1.82 M$_\odot$) and binary B (1.73 M$_\odot$). ^{c}Based on the AO imaging. ^{d}Based on a Monte Carlo selection of binary inclination angles and phases (see Section 11).

315 ± 50 pc. This distance estimate is therefore quite consistent with that found above from the brightness of binaries 'A' and 'B'.

11 BINARY 'C': COMPRISED OF BINARIES A AND B

Having established the basic properties of binaries 'A' and 'B', we can now consider them as likely bound members of a higher order binary (i.e. a quadruple star system) which we call 'C'. We know three quantitative things about the 'C' binary: (1) the relative RV of 'A' relative to 'B' is $\simeq$10.6 km s^{-1} as inferred from the difference in γ_A and γ_B, hereafter '$\Delta\gamma_{AB}$'; (2) the projected angular separation between these two components is $\simeq 0.095$ arcsec, based on the imaging study (see Section 9), which corresponds to a physical projected separation of $s \simeq 25 \pm 5$ au at the estimated distance of 260 ± 50 pc; (3) the relative radial acceleration of the two binaries with respect to each other is constrained to be $\lesssim$0.01 cm s^{-2} based on limits to $\dot{\gamma}$ for the 'A' and 'B' binaries (see Table 8). We can use these three facts to set some interesting constraints on the orbital period and inclination of the 'C' binary following the approach used in Lehmann et al. (2016) for the case of the quadruple system KIC 7177553.

Because we have only (i) the relative RV between the two binaries, $\Delta\gamma_{AB}$, (ii) a value for the projected physical separation, s, and (iii) an upper limit on the relative radial acceleration of the two binaries, we consider only the simple case of a circular orbit for the 'C' binary as being illustrative. These three quantities are related to the unknown orbital radius, a_C, inclination, i_C, and phase, ϕ_C by

$$s = a_C \sqrt{\cos^2 i_C + \sin^2 \phi_C \sin^2 i_C} \qquad (8)$$

$$\Delta\gamma_{AB} = \sqrt{\frac{GM_C}{a_C}} \sin\phi_C \sin i_C \qquad (9)$$

$$\dot{\gamma}_{AB} = \frac{GM_C}{a_C^2} \cos\phi_C \sin i_C, \qquad (10)$$

where M_C is the total system mass (i.e. the combined masses of binaries 'A' and 'B'). Note that ϕ_C is taken here to be zero at the time of superior conjunction, which is 90° from the definition used by Lehmann et al. (2016). Following Lehmann et al. (2016), this unknown orbital phase can be eliminated from equations (8) and (9) to find a cubic expression for the orbital separation:

$$a_C^3 \left(\frac{\Delta\gamma^2}{GM_C}\right) + a_C^2 \cos^2 i_C - s^2 = 0 \qquad (11)$$

In spite of the fact that we do not know the orbital inclination angle, i_C, we can still produce a probability distribution for a_C (and
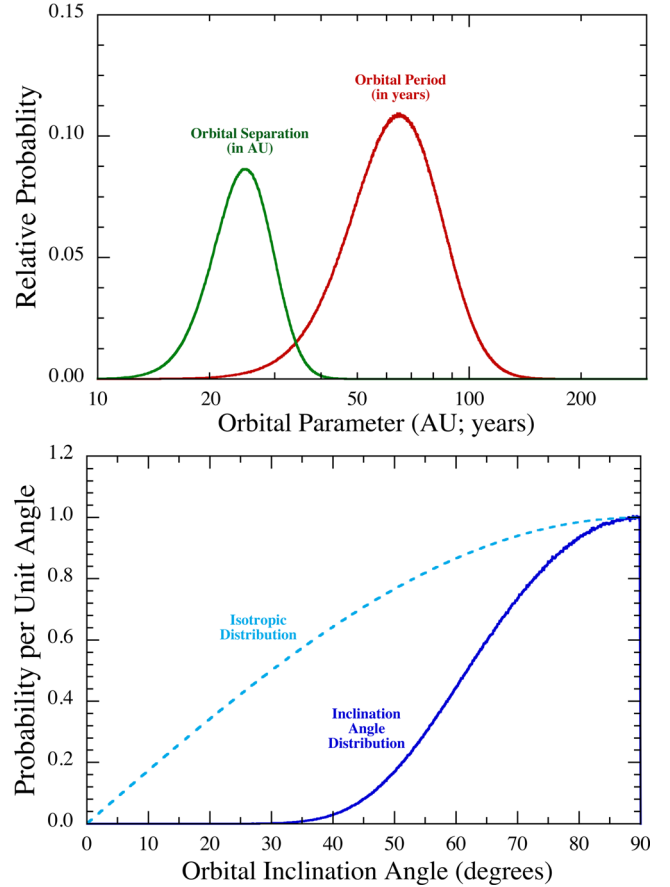
Figure 10. Top panel: orbital period distribution for binary 'C' (orbital period in red; orbital separation in green). Bottom panel: probability per unit orbital inclination angle for binary 'C'. The constraints are provided by $\Delta\gamma_{AB}$, the upper limit on $\dot{\gamma}_{AB}$, and the angular separation of binaries 'A' and 'B' (see summary in Table 8).

hence $P_{\text{orb,C}}$) via a Monte Carlo approach as follows. For each realization of the system, we choose a random inclination angle with respect to an isotropic set of orientations of the orbital angular momentum vector of the 'C' binary. In addition, because there is an uncertainty in the determination of $\Delta\gamma_{AB}$ (see Tables 4 and 5), and a significant uncertainty in the projected orbital separation, s (due largely to the uncertainty in distance to the target), we also choose specific realizations for those two quantities using a Gaussian random draw for both $\Delta\gamma_{AB}$ and s. We then solve equation (11) for a_C, and we also store the corresponding value of i_C. Finally, we restrict the inferred value of a_C so as to yield a value for the radial acceleration (see equation 10) that is lower than the observed upper limit cited in Table 8. If any inclination angle leads to a non-physical solution of equation (11), or a radial acceleration that is too large, we discard that system.

We repeat this process 10^8 times to produce our distributions of a_C, $P_{\text{orb,C}}$, and i_C. Probability distributions for $P_{\text{orb,C}}$, a_C, and i_C are shown in Fig. 10. The orbital period of binary 'C' is 65 ± 20 years (1σ uncertainties). The corresponding orbital separation is 25 ± 5 au. According to the orbital inclination angle distribution, values of $i_C \gtrsim 50°$ are strongly favoured (see bottom panel of Fig. 10). Such orbital periods are sufficiently short that the prospects for near-term detections of the accelerated motions of binaries 'A' and 'B' are highly promising.
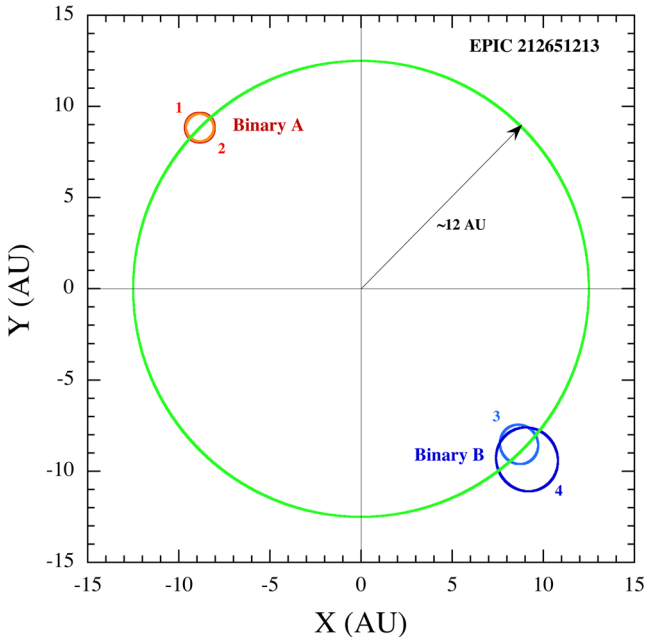
Figure 11. Schematic of the quadruple comprised of binaries 'A' and 'B' viewed from the orbital pole. The outer orbit of binary 'A' around binary 'B' is drawn to scale, the orbit is assumed circular, and the masses of the two binaries are taken to be equal (to within their uncertainties). The orbits of stars 1 and 2 in the circular binary 'A' and stars 3 and 4 in eccentric binary 'B' are drawn to the correct shape and size relative to each other; however, their absolute size has been artificially scaled up by a factor of ~20 so that the orbits can be resolved. The relative orbital speed of the 'A' and 'B' binaries would be about $10\,\mathrm{km\,s^{-1}}$ and the orbital period would be ~65 yr.

Given that the projected separation of binaries 'A' and 'B' on the sky is very similar (within the uncertainties) to the peak value of a_C in the distribution of orbital separation (see Fig. 10), i.e. $s \simeq a_C$ in equation (8), this implies that $\phi_C \simeq 90°$ or $270°$.

Repeating this exercise while allowing for eccentric orbits tends to broaden the distributions by a factor of about 2. We examined this question extensively in Lehmann et al. (2016). This would not change the conclusions reached here in a material way except to increase the uncertainties.

A sketch of the 'C' binary is shown in Fig. 11. The outer orbit of binary 'A' around binary 'B' is drawn to scale, and the orbit is assumed circular. The orbits of stars 1 and 2 in the circular binary 'A' and stars 3 and 4 in eccentric binary 'B' are drawn to the correct shape and size relative to each other; however, their absolute size has been artificially scaled up by a factor of ~20 so that the orbits can be resolved.

Since we are likely viewing binary 'C' with large inclination angles and $\phi_C \sim 90°$, we can reduce equations (8) and (9) to

$$\frac{\Delta s[\delta\phi_C]}{d_{\mathrm{pc}}} \sim 45\,\delta\phi_C^2 \text{ mas} \tag{12}$$

$$\Delta\gamma_{\mathrm{AB}}[\delta\phi_C] \sim 5\,\delta\phi_C^2 \text{ km s}^{-1}, \tag{13}$$

where d is the distance to the target, Δs is the change in projected physical separation (in au), and $\delta\phi_C$ is the advance in the orbital phase (in radians) over the next few years. Future RV and high-resolution imaging observations of this object should readily achieve accuracies of 1.5 mas in terms of the angular separation of binaries 'A' and 'B', and $1\,\mathrm{km\,s^{-1}}$ for the RV measurements. Solving

for the orbital phase changes required to make a detection of orbital motion in binary 'C' we find $\delta\phi_C \simeq 0.03$ and 0.07 orbital cycles for the high-resolution imaging and the RV observations, respectively. These orbital phase advances correspond to ~2 and 4.5 yr, respectively. Thus, we advocate further RV and high-resolution imaging of this object starting a couple of years from now.

12 E1213 AND E1234 AS A BINARY PAIR

The three facts we have to work with concerning the relationship between objects E1213 (comprised of a quadruple star system) and E1234 (which appears single both in imaging and spectroscopy), are the following. First, the projected separation of the two stars is 10.56 arcsec on the sky. For a distance of about 260 pc, this corresponds to a projected physical separation of about 2800 au or 0.013 pc. This is well within the allowed separation for stars to remain bound pairs without being tidally disrupted in their passage around the Galaxy (Jiang & Tremaine 2010). Secondly, the RV of the centre of mass of the 'C' binary (actually a quadruple system) is $-13.6\,\mathrm{km\,s^{-1}}$ while the RV of E1234 is $-15.0\,\mathrm{km\,s^{-1}}$, both with an uncertainty of $\sim1\,\mathrm{km\,s^{-1}}$. These are suggestively close to having the same value. Thirdly, the magnitude of the difference in the two proper motion vectors is only 3.4 ± 2.3 mas yr^{-1}.

Combining these three facts leads to the quite plausible, even highly likely, notion that E1213 and E1234 are themselves a gravitationally bound binary pair. We refer to this as the 'D' binary. The angular, velocity, and time-scales are too long to hope to see any changes in this binary over the next decades.

13 E1234 AS A SINGLE STAR

The rms scatter of the RVs for E1234 within the combined TRES and KO sets is ~100 m s^{-1}, while for the TLS observations by themselves, the rms scatter is similar (see Table 3). However, there is a systematic offset between these two sets of ~900 m s^{-1}. If we subtract off that constant offset from the three TLS RV measurements of E1234, the overall rms spread in the RV measurements remains at 100 m s^{-1}. We are unable to account for the systematic shift between observatories, which has minimal effect on the evaluation of the orbital parameters in binaries 'A' and 'B'. However, for estimating an upper limit to the projected radial acceleration of a possible binary in E1234 this discrepancy matters, and we adopt an rms RV of 100 m s^{-1} for this purpose. In turn, this yields an upper limit to the projected radial acceleration of ~0.003 cm s^{-2}.

In addition, the angular separation of any internal stellar pairs is $\lesssim0.05$ arcsec based on the AO and speckle imaging (see Section 9).

The limits on angular separation and projected radial accelerations suggest that any binary stellar pair within E1234 has a physical separation, a constrained by

$$20\sqrt{\sin i \cos\phi} \lesssim a \lesssim 13\left(\cos^2 i + \sin^2\phi\,\sin^2 i\right)^{-1/2} \text{au}, \tag{14}$$

where i and ϕ are the orbital inclination angle and phase, respectively, of any hypothetical binary in E1234 (as in equations 8 and 10). Here we have assumed a total binary mass of $2\,\mathrm{M_\odot}$.

Interestingly, unless the orbital phase or inclination angle are somewhat finely tuned, the above constraints already suggest that any putative binary in E1234 must have an orbital separation not too far from ~16 au. If it is much wider it would have been resolved with AO or speckle imaging, and if much closer the acceleration (i.e. change in γ velocity) would likely have been detected over the 72-d interval of the RV measurements.

To push this argument a bit further, we took advantage of TRES's 15 m s^{-1} instrumental stability. Relative RVs were derived by cross-correlating each observed spectrum, order-by-order, against the strongest observed spectrum over the wavelength range 0.435–0.628 μm. These yield significantly tighter constraints on *changes* in velocity over the course of the observations than the absolute velocities given in Table 3. With these multi-order velocities, we can set a limit of ≈30 m s^{-1} on the constancy of the RV for E1234. In turn, this lower limit increases the coefficient on the left-hand side of equation (14) to a value of ∼35. This constraint effectively eliminates nearly all viable solutions for the semimajor axis of any putative circular binary. All this is in keeping with our assertion that image E1234 is that of a single star.

Finally, we note that if the location of star E1234 in the log g − T_{eff} is as shown in Fig. 6, it is significantly evolved, and would have a mass of $\lesssim 1.3\,M_\odot$ and an age $\gtrsim 4.4$ Gyr. If we take E1213 and E1234 to be coeval, this sets the same lower limit to the age of the two binaries in E1213.

14 SUMMARY AND CONCLUSIONS

We have presented an unusual quintuple star system consisting of five stars arranged as a hierarchical quadruple orbited by a single star. The K2 data show that both binaries comprising the quadruple are eclipsing (Fig. 3). We have measured the spectroscopic orbits of three of the four stars in the two binaries (Fig. 5). The 5-d binary is highly circular, while the 13-d binary is eccentric with $e_B \simeq 0.32$ (Fig. 5 and Tables 4 and 5). The separation of the two binaries is resolved by both Keck AO imaging and WIYN speckle interferometry at 90 mas (Fig. 9). The flux ratio of the two binaries was thereby measured quite accurately at four different wavelengths with the AO and speckle imaging (Table 7). By combining the three measured mass functions with the flux ratio of binary 'B' to 'A', and utilizing stellar evolution models, we have managed to extract reasonably accurate stellar parameters for all four stars in the two binaries (Fig. 7).

We have shown that if the RV and/or high-resolution imaging of this object are repeated 2–3 yr from now, there is a good chance that changes in the motion of binary 'A' with respect to binary 'B' (i.e. within the binary 'C' system) will be detected. Additionally, in regard to detecting motion within the 'C' binary, we note that the eclipses of binary 'A' are deep enough to easily follow from ground-based observations. If the eclipses can be tracked with an accuracy of minutes, then we should be able to detect significant eclipse timing variations within a few years. This is physically equivalent to measuring $\dot{\gamma}_{AB}$ via RV observations.

After analysing and evaluating the quadruple system E1213, we argued that the stellar image E1234 is itself a single star (see Section 13), and is very likely bound to the quadruple system (see Section 12).

This system is one of only a relative handful of known quadruple or higher multiplicity stellar systems where the RVs have been measured for both binaries, and where, additionally, both binaries are eclipsing. It has a short enough outer orbital period so that motion of that longer period system can be detected within a few years.

ACKNOWLEDGEMENTS

REFERENCES

Ahn C. P. et al., 2012, ApJS, 203, 21
Asplund M., Grevesse N., Sauval A. J., Scott P., 2009, ARA&A, 47, 481
Barstow M. A., Bond H. E., Burleigh M. R., Holberg J. B., 2001, MNRAS, 322, 891
Batalha N. M. et al., 2011, ApJ, 729, 27
Borkovits T., Rappaport S., Hajdu T., Sztakovics J., 2015, MNRAS, 448, 946
Borkovits T., Hajdu T., Sztakovics J., Rappaport S., Levine A., Bíró I. B., Klagyivik P., 2016, MNRAS, 455, 4136
Borucki W. J. et al., 2010, Science, 327, 977
Buchhave L. A. et al., 2010, ApJ, 720, 1118
Buchhave L. A. et al., 2012, Nature, 486, 375
Claret A., Bloemen S., 2011, A&A, 529, A75
Conroy K. E., Prša A., Stassun K. G., Orosz J. A., Fabrycky D. C., Welsh W. F., 2014, AJ, 147, 45
Cutri R. M. et al., 2013, Explanatory Supplement to the AllWISE Data Release Products
Derekas A. et al., 2016, MNRAS, in press
Di Folco E. et al., 2014, A&A, 565, 2
Fabrycky D., Tremaine S., 2007, ApJ, 669, 1298
Hadrava P., 1995, A&AS, 114, 393
Hadrava P., 2004, in Hilditch R. W., Hensberge H., Pavlovski K., eds, ASP Conf. Ser. Vol. 318, Spectroscopically and Spatially Resolving the Components of the Close Binary Stars. Astron. Soc. Pac., San Francisco, p. 86
Horch E. P., Veillette D. R., Baena Gallé R., Shah S. C., O'Rielly G. V., van Altena W., 2009, AJ, 137, 5057
Horch E. P., Gomez S. C., Sherry W. H., Howell S. B., Ciardi D. R., Anderson L. M., van Altena W. F., 2011, AJ, 141, 45
Howell S. B., Everett M. E., Sherry W., Horch E., Ciardi D. R., 2011, AJ, 142, 19
Howell S. B. et al., 2014, PASP, 126, 398
Huber D. et al., 2016, ApJS, 224, 2
Hut P., 1981, A&A, 99, 126
Ilijic S., 2004, in Hilditch R. W., Hensberge H., Pavlovski K., eds, ASP Conf. Ser. Vol. 318, Spectroscopically and Spatially Resolving the Components of the Close Binary Stars. Astron. Soc. Pac., San Francisco, p. 107

Jiang Y.-F., Tremaine S., 2010, MNRAS, 401, 977

Kirk B. et al., 2016, AJ, 151, 68

Kiseleva L. G., Eggleton P. P., Mikkola S., 1998, MNRAS, 300, 292

Kozai Y., 1962, AJ, 67, 591

Kupka F, Piskunov N., Ryabchikova T. A., Stemples H. C., Weiss W. W., 1999, A&AS 138, 119

Kurucz R. L., 1992, in Barbuy B., Renzini A., eds, Proc. IAU Symp. 149, The Stellar Populations of Galaxies. Kluwer, Dordrecht, p. 225

LaCourse D. M. et al., 2015, MNRAS, 452, 3561

Lehmann H. et al., 2011, A&A, 526, 124

Lehmann H., Zechmeister M., Dreizler S., Schuh S., Kanzler R., 2012, A&A, 541, 105L

Lehmann H., Borkovits T., Rappaport S., Ngo H, Mawet D., Csizmadia Sz., Forgács-Dajka E., 2016, ApJ, 819, 33.

Lidov M. L., 1962, Planet. Space Sci., 9, 719

Lohr M. E. et al., 2015, A&A, 578, 103L

Matijevič G., Prša A., Orosz J. A., Welsh W. F., Bloemen S., Barclay T., 2012, AJ, 143, 123

Moreno E., Koenigsberger G., Harrington D. M., 2011, A&A, 528, A48

Ngo H. et al., 2015, ApJ, 800, 138

Raghavan D. et al., 2009, ApJ, 690, 394

Rappaport S., Deck K., Levine A., Borkovits T., Carter J., El Mellah I., Sanchis-Ojeda R., Kalomeni B., 2013, ApJ, 768, 33.

Schütz O., Meeus G., Carmona A., Juhász A., Sterik M. F., 2011, A&A, 533, 54

Service M., Lu J. R., Campbell R., Sitarski B. N., Ghez A. M., Anderson J., 2016, PASP, 128, 967

Shibahashi H., Kurtz D. W., 2012, MNRAS, 422, 738

Shulyak D., Tsymbal V., Ryabchikova T., Stütz C., Weiss W. W., 2004, A&A, 428, 993

Simon K. P., Sturm E., 1994, A&A, 281, 286

Skrutskie M. F. et al., 2006, AJ, 131, 1163

Slawson R. W., Prša A., Welsh W. F., 2011, AJ, 142, 160

Still M., Barclay T., 2012, Astrophysics Source Code Library, record ascl:1208.004

Szentgyorgyi A.-H., Furész G., 2007, Rev. Mex. Astron. Astrofis. Ser. Conf., 28, 129

Tkachenko A., Lehmann H., Smalley B., Debosscher J., Aerts C., 2012, MNRAS, 422, 2960

Tokovinin A., 2016, AJ, 152, 10

Torres G., 2006, AJ, 131, 1702

Tsymbal V., 1996, in Adelman S. J., Kupka F., Weiss W. W., eds, ASP Conf. Ser. Vol. 108, M.A.S.S.; Model Atmospheres and Spectrum Synthesis. Astron. Soc. Pac., San Francisco, 198

Yi S., Demarque P., Kim Y.-C., Lee Y.-W., Ree C. H., Lejeune T., Barnes S., 2001, ApJS, 136, 417

Zacharias N., Finch C. T., Girard T. M., Henden A., Bartlett J. L., Monet D. G., Zacharias M. I., 2013, ApJS, 145, 44

Zahn J.-P., 2008, in Goupil M.-J., Zahn J.-P., eds, EAS Publ. Ser. Vol. 29, Tidal Effects in Stars, Planets and Disks. p. 67

Zasche P., Uhlař R., 2016, A&A, 588, 121

This paper has been typeset from a TEX/LATEX file prepared by the author.